# A numerical investigation of high-resolution multispectral absorption tomography for flow thermometry

**Weiwei Cai · Clemens F. Kaminski**

**Abstract** Multispectral absorption tomography (MAT) is now a well-established technique that can be applied for the simultaneous imaging of temperature, species concentration, and pressure of reactive flows. However, only intermediate spatial resolution, on order of $15 \times 15$ grid points, has so far been achievable in previous demonstrations. The aim of the present work is to provide a numerical validation of our MAT algorithm for thermometry of combusting flows, but with greatly improved spatial resolution to motivate its experimental realization in practical environments. We demonstrate a grid resolution that is comparable to that of classical absorption tomography (CAT) containing $80 \times 80$ elements from only two orthogonal projections, which is impractical to realize with CAT but especially desirable for applications where optical access is limited. This is achieved using the smoothness assumption, which holds true under most combustion conditions. The study shows that better spatial resolution can be obtained through a simple increase in the spatial sampling frequency for the two available projections, as the smoothness condition becomes more reliable on smaller spatial scales. Our work also demonstrates the first application of MAT for full volumetric reconstructions. The studies thus provide robust guidelines for the implementation of MAT over large spatial scales and lay solid foundations for its development and application in complex technical combustion scenarios,
where spatial resolution is crucial to investigate the interaction of flow phenomena with chemical reactions.

## 1 Introduction

Optical imaging techniques are indispensable for the resolution of non-uniformities in technical flow fields [1, 2]. Generally the techniques can be divided into two categories, which are planar imaging techniques on the one hand and tomography, on the other. As evident from its name, the former category, which includes planar laser-induced fluorescence/phosphorescence [3, 4] and Raman/Rayleigh imaging [5–7], is two-dimensional in nature and requires a pulsed laser source for the selective illumination of the plane of interest. The signal stems from the interaction of the illumination light field with the gas molecules, and the generated light emission is imaged directly onto a two-dimensional detector array, typically a camera. Mathematically speaking, planar imaging techniques can be considered as a straightforward linear field mapping operation. On the other hand, tomography relies on the mapping of integrals of the target field along the line of sight, LOS, which in what follows we refer to as integral mapping [8]. As a consequence, the target field has to be integratable along the LOS and the corresponding integrals have to be physically meaningful. Since emission along the LOS is accumulative and hence integratable along its path toward the detection plane, essentially all planar imaging methods can be upgraded into 3D tomographic modalities. In practice, limitations are only set by the available optical access to the system under study and the excitation power available for volumetric sample illumination. In contrast to planar imaging, which solely targets on emission fields, tomography can also recover the fields for absorption coefficients,

W. Cai · C. F. Kaminski (✉)
Department of Chemical Engineering and Biotechnology,
University of Cambridge, Cambridge CB2 3RA, UK
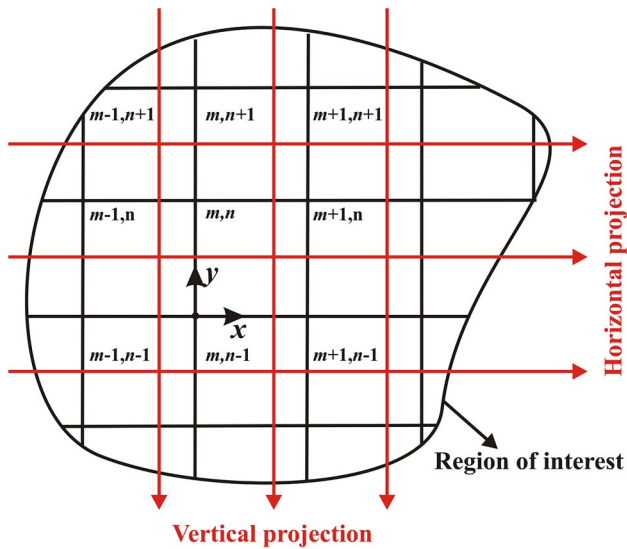e-mail: cfk23@cam.ac.uk

**Fig. 1** Geometric arrangement of a typical MAT experimental setup

which can be further processed to retrieve other fundamental gas properties, such as temperature, species concentration, and pressure [9–14]. Compared with emission tomography, the absorption counterpart enjoys further advantages such as being calibration free, species selective, and highly sensitive [15–20].

Tomographic absorption techniques can be further classified into classical and nonlinear methods depending on the sampling schemes and mathematical algorithms employed [8]. Classical absorption tomography, CAT, can only handle a single absorption transition in the inversion process, and thus, extensive sampling is required to obtain the number of projections (the sets of line-of-sight measurements along specified orientations) necessary for high-resolution reconstruction. Such a sampling scheme usually requires mechanical means for the angular displacement of the projections, which inevitably undermines the temporal resolution, making it unsuitable for rapidly evolving turbulent flows. Since CAT results in a set of linear equations, we also refer to it as linear tomography. On the other hand, nonlinear methods are inherently multiplexed: For example, the MAT technique reported previously measures

several spectral sampling frequencies simultaneously but on the other hand requires only two spatial projections, and it is thus inherently faster than CAT [12, 15]. It was demonstrated before that with two fixed orthogonal projections, a faithful tomographic reconstruction can be obtained for a sample containing 15 × 15 resolution elements at MHz repetition rates [12, 15]. The geometric arrangement of a typical MAT experimental setup with two orthogonal projections is illustrated in Fig. 1. A schematic comparison of the sampling schemes used for CAT and MAT is summarized in Fig. 2. As illustrated, three measurement dimensions are involved, which are: angular (i.e., # of projections), lateral (i.e., # of sampling beams within a specific projection), and spectral dimension, respectively. The relative lengths of the axes indicate the intensiveness of the sampling operation along a specific dimension.

However, since only two projections were used in previous implementations of MAT and the spectral sampling could only partially compensate (in a mathematical sense) for spatial sampling deficiencies, the spatial resolution is inevitably undermined. Nevertheless, we point out that there is no limitation *per se* in the number of projections that can be accommodated by the MAT algorithm, however, at a commensurate loss in temporal resolution due to beam scanning requirements. But in this case, MAT enjoys a much improved reconstruction fidelity due to better immunity against experimental noise such as originating from beam steering, window fouling, and etalon fringing [15]. Moreover, since MAT can be combined with advanced detection techniques, such as wavelength modulation spectroscopy (WMS), it can be used for high- and/or varying pressure scenarios, for which CAT is not optimally suited. In summary, the nonlinear MAT technique offers full flexibility, to either be deployed with high temporal but somewhat limited spatial resolution, as demonstrated in an earlier article, or, as we demonstrate here, at very high spatial resolution at the cost of increased data acquisition requirement.

We demonstrate this effect by increasing the spatial sampling frequency along each projection direction. This finer meshing of the flow filed is permissible under the assumption of the smoothness condition, which is valid for most
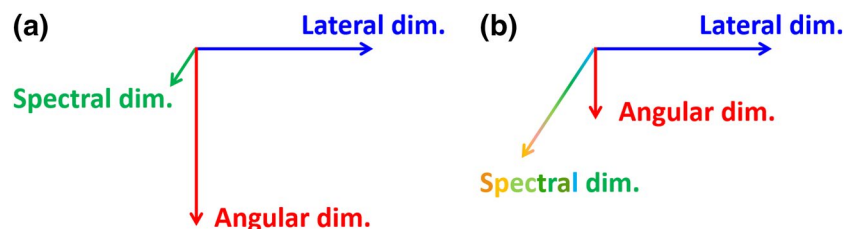


**Fig. 2** Schematic comparison of the dimensionality of sampling schemes for, **a** classical absorption tomography and **b** multispectral absorption tomography. The relative lengths of the axes indicate the intensiveness of the sampling process along a specific dimension

combustion environments practically encountered. We demonstrate a resolution spatially for grid sizes containing $80 \times 80$ elements to achieve a resolution that is comparable to that of CAT although requiring only a fraction of projections. For high-resolution MAT, the temporal resolution is furthermore only limited by the bandwidth of the data acquisition system. High-resolution MAT has thus the practical potential for deployment in situations where both spatial and temporal resolutions are crucial, for example to provide full resolution of complicated flow fields such as supersonic combustion systems within ramjets/scramjets [21].

So far, both CAT and MAT have been limited to applications in two dimensions, simply because of prohibitive experimental costs for the enabling technology. However, the potential for the implementation of MAT with inexpensive tunable diode lasers with coarse wavelength-division multiplexing (CWDM) [15] has made volumetric absorption tomography a more practical proposition. This provides us with a strong motivation to further develop this technique theoretically and perform numerical validation studies in preparation for experimental demonstrations in the near future.

The remainder of this paper is organized as follows: Sect. 2 briefly introduces the mathematical formulation for the MAT algorithm; Sects. 3 and 4 present studies for large-scale planar and volumetric implementations of the technique, and the final section provides a summary of our findings.

## 2 Mathematical formulation of MAT

The mathematical formulation of MAT using both direct absorption spectroscopy (DAS) and WMS has been detailed in previous publications [15, 22]. To facilitate the discussion here, we focus on MAT implementations based on DAS as an example and briefly summarize the formulation to use MAT for flow thermometry.

According to the Beer–Lambert law, the absorbance, labeled as $\alpha$, for monochromatic light of a frequency $v$ passing through *non-homogeneous* absorbing medium is defined as:

$$\alpha(v) = \int_{L_1}^{L_2} \sum_g S[T(l), v_g] \cdot \phi[T(l), X(l), P, (v_g - v)] \cdot P \cdot X(l)$$

$$(1)$$

where $L_1$ and $L_2$ the intersections between the laser beam and the boundaries of the region of interest, ROI; $T(l)$ and $X(l)$ the temperature and concentration profiles along the LOS as a function of distance, $l$; $P$ the pressure; $\phi$ the normalized Voigt line-shape function, which approximates the convolution of the two dominant broadening mechanisms,

i.e., Doppler and collisional broadening, representative for typical combustion scenarios; and $S[T(l), v_g]$ is the line strength of the $g$th non-negligible transition centered at $v_g$ and for prevailing local temperature $T(l)$. In practice, the ROI is represented by discretized pixels, and the integration in the equation is replaced by a summation operation.

In MAT, the left-hand side of Eq. (1) can be obtained from experimental measurements and the right-hand side can be predicted using Beer's law. By taking LOS measurements at different lateral positions and orientations across the sample for multiple absorption transitions, which is achieved by coarse/dense wavelength-division multiplexing (CWDM/DWDM), the parameters are obtained for a set of nonlinear equations, whose common variables are the profiles of temperature and species concentration. Here we assume that the pressure is constant, which is the case for many practical applications. Currently, the standard way of solving the MAT equation system is through iterative optimization via minimization of a cost function, defined as

$$D = \sum_{j=1}^{J} \sum_{i=1}^{I} \left[ 1 - p_c(\ell_j, v_i, T_q, X_q)/p_m(\ell_j, v_i) \right]^2 \quad (2)$$

where $I$ denotes the total number of peak wavelengths used; $J$ the number of sampling laser beams within ROI; $p_m(l_j, v_i)$ the LOS measurements at the frequency $v_i$ along the $j$th laser beam; and $p_c(l_j, v_i)$ the corresponding predictions using Beer's law. The cost function, $D$, provides a quantitative measure of the difference between the fitted and measured projections. In the ideal case, where measurements are noise-free and the spectroscopic database is accurate, $D$ reaches its global minimum (zero) when the reconstructions match the true profiles. However, in reality due to the noisy projections, numerous local minima that have values close to the global minimum would lead to solutions that are significantly different from the true profiles. In this case, additional constraints such as smoothness conditions due to thermal and mass diffusion can be incorporated into the inversion process to rule out the solutions that disagree with the constraints so that a smooth solution which serves as a good approximate of the true profiles can be reached. For example, the smoothness of temperature within the ROI can be implemented as:

$$R_T\left( \overrightarrow{T}^{\text{rec}} \right) = \sum_{m=1}^{M} \sum_{n=1}^{N} \left[ \sum_{i=m-1}^{m+1} \sum_{j=n-1}^{n+1} \left( T_{i,j}^{\text{rec}} - T_{m,n}^{\text{rec}} \right)/8 \right] \quad (3)$$

where $\overrightarrow{T}^{\text{rec}}$ stands for the reconstructed temperature distribution; $M$ and $N$ the number of square pixels along the $x$ and $y$ directions, respectively; the subscript $m$, $n$ run over all inner pixels within the ROI; and the subscripts $i$, $j$ enumerate the immediate adjacent pixels to every pixel specified by $m$ and $n$.

Obviously, $R_T$ decreases as the distribution becomes smoother, and for a constant temperature field, $R_T$ would approach zero. The cost function can thus be modified as

$$F = D + \gamma_T \cdot R_T(T^{rec}) \tag{4}$$

where $\gamma_T$ is a weighting parameter to regulate the relative significance of a priori (smoothness of the temperature profile) and *posteriori* (measured projections) information. Since it was previously demonstrated that the recovery of temperature information in the MAT process is only weakly affected by local concentration variations [23], we omit the latter in the formulation for $F$. However, it has to be pointed out that both the temperature and concentration profiles were set as independent free variables during the fitting process. The minimization problem can then be solved using a global minimizer, e.g., the simulated annealing (SA) algorithm [24], which we use here.

## 3 Large-scale planar MAT

For the study of large-scale planar MAT problems, we artificially generated smooth, but multi-modal 2D phantoms of flame temperature and water vapor concentration as shown in Fig. 3 in order to simulate practical flow conditions. Water vapor was chosen as the target species due to its relatively strong absorption in the near-infrared spectral region compared with other flame species and also due to its abundance in hydrocarbon/hydrogen flames. For practical applications, the continuous phantoms are meshed by a grid containing $N \times M$ pixels. Here we vary $N$ and $M$ to study the effect of variations in the spatial sampling frequency along the projections on the MAT reconstruction quality. Typically both forward and backward projection processes were considered, i.e., going from phantom to projections and vice versa. In the forward process, the noise-free projections were modeled according to Beer's law assuming that an accurate spectroscopic database had been used. A specified level of noise was then added to

simulate practical projections suffering from noise (*posterior* information). In the backward process, a large number of trial solutions were generated within constraints to match the fitted projections calculated via Eq. (1) to the 'measured' projections, while at the same time, ensuring the smoothness condition was met (a priori information). The optimal solution was then taken to be that which struck the best balance between a priori and *posterior* constraints. To quantify reconstruction quality, an overall average error was defined as follows

$$e_T = || \vec{T}^{rec} - \vec{T}^{true} ||_1 / || \vec{T}^{true} ||_1 \tag{5}$$

where $\vec{T}^{true}$ is the temperature phantom arranged in a vector form and $|| \, ||_1$ denotes the Manhattan norm of a vector.

Figure 4 shows the reconstruction results for a typical case with $N = M = 60$. Two orthogonal projections, each containing 60 laser beams, were assumed so that each projection passed through each grid pixel once. Twenty strong $H_2O$ absorption transitions in the 1,350- to 1,500-nm spectral range were selected for this demonstration. Gaussian noise was added at 5 % of the peak value to each projection to simulate the realistic experimental conditions. Thus ca ~2,000 nonlinear equations were obtained from the simulated measurements. For the case where we modeled the system to contain two unknown variables (i.e., temperature and water vapor concentration) for each pixel, an equation system containing ca ~7,000 variables was obtained. The results for the final reconstructed temperature profiles are shown in Fig. 4, left panel. Clearly, the major features of the systems are recovered with good resolution, e.g., the twin peak system of the temperature profile. The average error obtained is only 1.39 % (~25 K). It has to be noted that the lower reconstruction quality on the edge is due to the relatively weak enforcement of the regularization since the pixels on the edge have fewer adjacent pixels available for smoothing. The right panel in Fig. 4 shows the evolution of the terms contributing to the cost function as the SA algorithm progresses, i.e., $D$ and $\gamma_T \cdot R_T(T^{rec})$ normalized



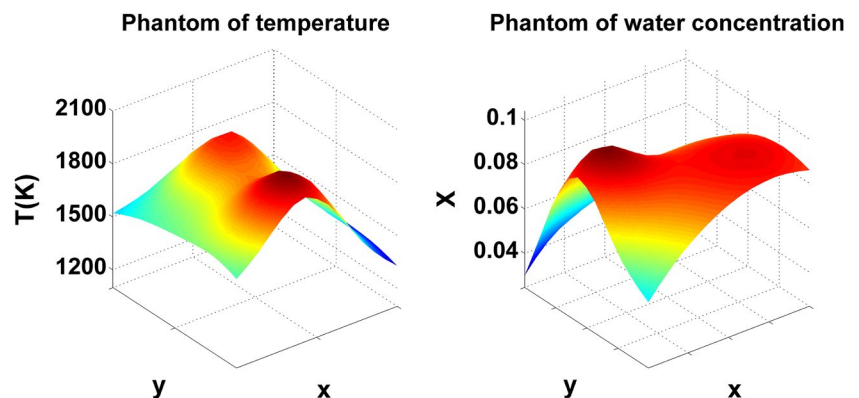**Fig. 3** Continuous phantoms generated to simulate temperature and water vapor concentrations in a combusting flow

**Fig. 4** An example reconstruction using a discretization of $60 \times 60$ grid points. See also Media 1 for an animation for the evolution of the reconstructed temperature distribution and the cost function as the Simulated Annealing algorithm progresses. 5 % Gaussian noise was added to all projections to simulate realistic noise conditions as may be encountered in practical experiments
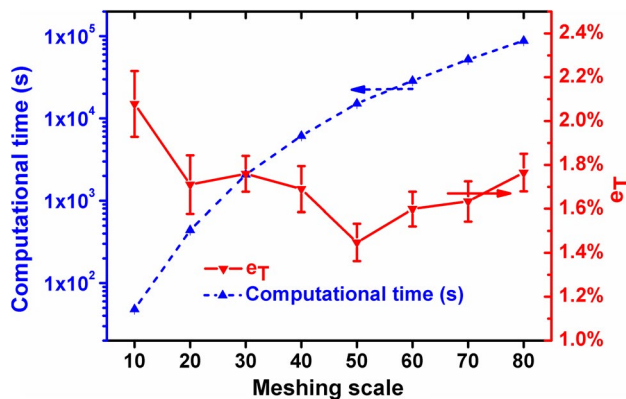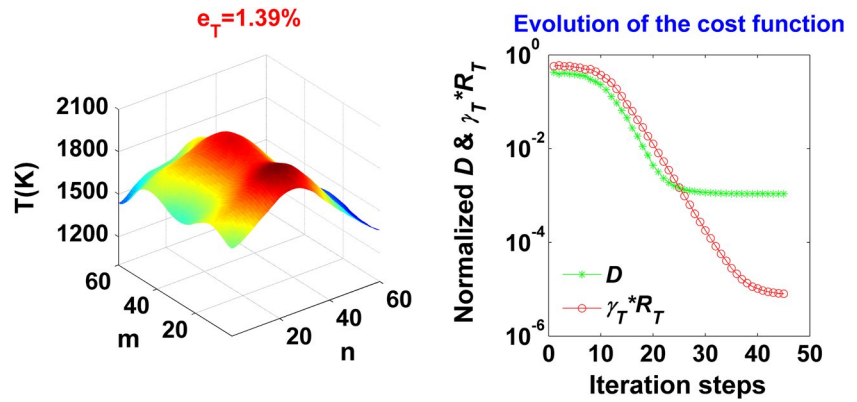
**Fig. 5** Reconstruction error of temperature profile and corresponding computational time as a function of meshing scale. 5 % Gaussian noise was added to all projections

by the initial value of $F$. As can be seen already halfway through the fitting process, the cost function (green symbols) has essentially reached its minimum, indicating a close resemblance between fitted and "measured" projections. On the other hand, the regularization term (red symbols) continues to decrease until the termination criterion is satisfied in the procedure. This means there were numerous temperature profiles that lead to the similar "measured" projections, but only the smooth profiles result in a small regularization term. The procedure guarantees a smooth solution as the best approximation to the true phantom. The evolution of both the fitted temperature profile and the contribution terms in the cost function guided by the SA algorithm can be found in Media 1.

Figure 5 shows the reconstruction error of temperature ($e_T$) and the corresponding computational time as a function of meshing scale. The same simulation conditions, i.e., the number of projections, transitions, and noise levels in the "measurements" were used as for the case shown in Fig. 4. To make the comparison meaningful, all simulations were run on the same Intel Core i7-4770 Processor. The error bars here indicate the standard deviation of 30 cases

using projections with the same noise levels. It is seen that the computational time increases almost exponentially with meshing frequency which is explained by the fact that the number of free variables in the optimization is $2 \times N \times M$. Furthermore, $e_T$ decreases with meshing grid sizes up to $50 \times 50$ and increases thereafter. This is due to the fact that the smoothness condition is better satisfied for finer discretization; however, as the meshing scale is increased beyond a critical value, the ratio between the number of variables and nonlinear equations ($N/I$) also increases, thus reducing reconstruction quality. The overall reconstruction fidelity represents an amalgamation of both factors. For small meshing scales, the smoothness condition will outweigh the effect of increasing $N/I$ and vice versa.

## 4 Volumetric MAT

So far, MAT, and indeed CAT, has been limited to 2D situations simply due to prohibitive experimental costs. Fortunately, recent advances in MAT with inexpensive tunable diode lasers have made the experimental realization of volumetric absorption tomography a more realistic proposition. This is what encourages us to perform preliminary numerical studies here in preparation for later experimental demonstrations. We note that volumetric MAT implementation is a worthwhile endeavor not only from an application point of view (i.e., providing full 3D information for the system under study), but it brings advantages also for tomographic inversion process, because extra information gained along directions between adjacent planes offers further constraints (e.g., smoothness between the layers) that make the method even more robust.

Here we test the feasibility of such a volumetric tomography approach with MAT. We thus generated a 3D phantom as shown in Fig. 6 in such a way that the smoothness condition could be applied not only within, but also between the layers. The ROI was discretized into $15 \times 15 \times 15$ voxels, and thus, there are totally ~7 k

**Fig. 6** Volumetric temperature phantom using a discretization of 15 × 15 × 15
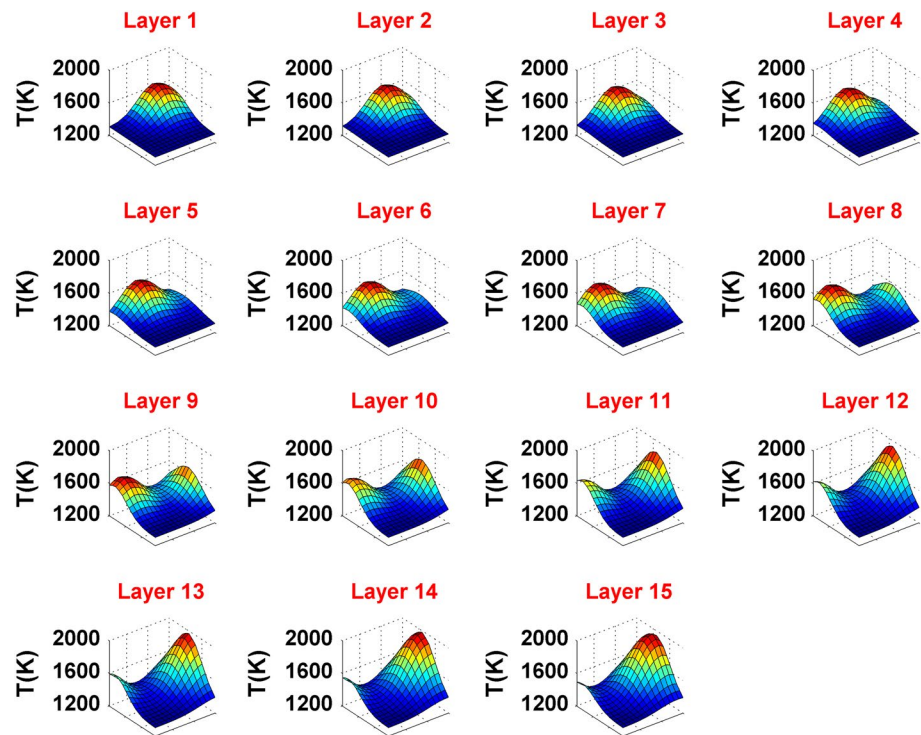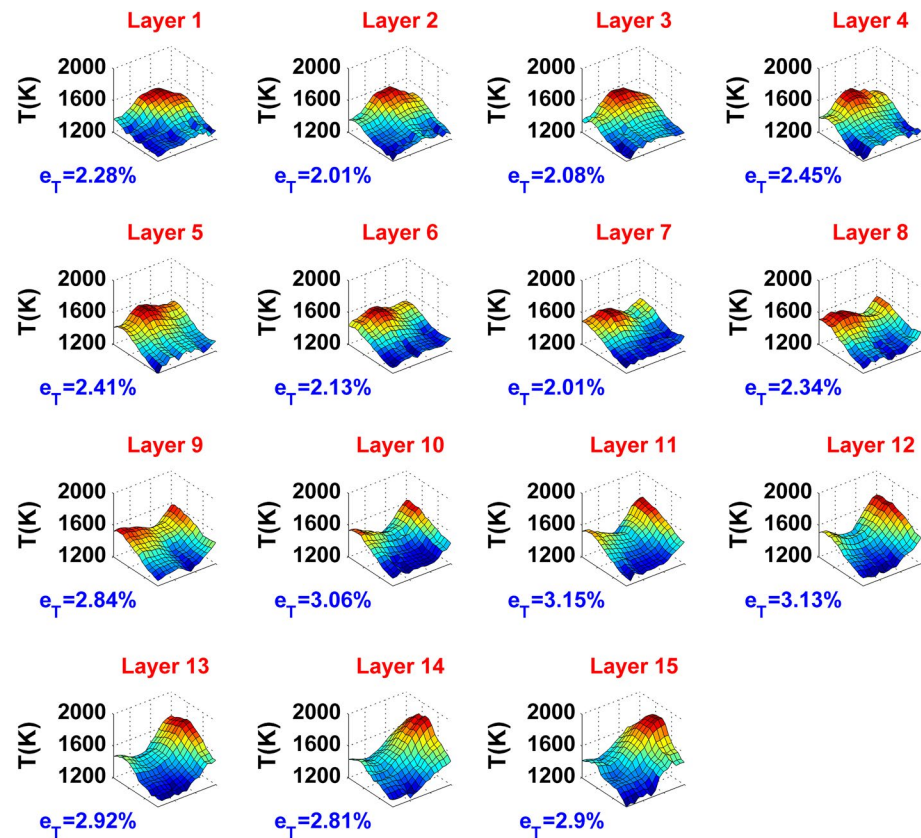


**Fig. 7** Reconstructed volumetric temperature distributions. Average temperature errors $e_T$ are indicated for each reconstructed layer

variables (i.e., 3,375 for temperature and 3,375 for species concentration). Again the same simulation conditions were used as in the planar MAT cases. Two orthogonal projections were assumed, with 450 beams thus resulting in exactly 9,000 nonlinear equations. Accordingly, Eq. (2) was modified to accommodate measurements along the third dimension as:

$$D = \sum_{k=1}^{K}\sum_{j=1}^{J}\sum_{i=1}^{I}\left[1 - p_c(\ell_{j,k}, v_i, T_q, X_q)/p_m(\ell_{j,k}, v_i)\right]^2 \quad (6)$$

where $K$ indicates the total number of layers.

In addition, to take full advantages of connections between layers, Eq. (3) was rewritten as:

$$R_T\left(\vec{T}^{rec}\right) = \sum_{k=1}^{K}\sum_{m=1}^{M}\sum_{n=1}^{N}\left[\sum_{g=k-1}^{k+1}\sum_{i=m-1}^{m+1}\sum_{j=n-1}^{n+1}\left(T_{g,i,j}^{rec} - T_{k,m,n}^{rec}\right)/26\right]$$
$$(7)$$

Figure 7 shows an example reconstruction of the volumetric temperature field for the phantom. The average error $e_T$ is stated for each recovered layer in the figure panels. Remarkably, a good reconstruction fidelity was obtained with an overall errors $e_T$ of <2.6 % (~40 K) throughout.

## 5 Conclusion

In summary, we present the numerical studies of nonlinear MAT for large computational mesh sizes. We demonstrate a spatial resolution with meshes containing up to $80 \times 80$ grid points for planar MAT requiring just two orthogonal projections. The spatial resolution obtained is comparable with that of CAT, which needs many more projections. Even better spatial resolution is in principle possible at the expense of increased computational cost. We show that reconstruction fidelity is improved simply by increasing the spatial sampling frequency along the available orthogonal projections before the effect of increasing $N/I$ (the ratio between the number of variables and nonlinear equations) outweigh the benefit of smoothness condition. However, it has to be pointed out that for more complicated turbulent flow fields featuring sharper gradients and more intense fluctuations, more projections are necessary to resolve all information on relevant spatial scales. In theory, resolution can be improved by using more projections, but in practice, the achievable resolution is dictated by the maximum number of projections available with limited optical access and the optimal signal noise ratios that are possible. An advantage of the MAT algorithm is that it features a better noise immunity when the same number of projections was used as CAT against experimental noise originating from beam steering, window fouling, and etalon fringing [15]. Finally,

we demonstrate that full volumetric MAT is a feasible and realistic proposition for experimental realization. The availability of cost efficient laser and detector technologies mean that full 3D reconstructions of dynamic combusting flows will soon become a reality.

## References

1. M.A. Linne, *Spectroscopic measurement: an introduction to the fundamentals* (Academic Press, London, 2002)
2. K. Kohse-Höinghaus, J.B. Jeffries, *Applied combustion diagnostics* (Taylor & Francis, New York, 2002)
3. B. Peterson, E. Baum, B. Böhm, V. Sick, A. Dreizler, P. Combust, Inst. **34**, 3653 (2013)
4. M. Mosburger, V. Sick, M. C. Drake, Int. J. Engine Res., 1468087413476291 (2013)
5. U. Doll, G. Stockhausen, C. Willert, Exp. Fluids **55**, 1 (2014)
6. D. Hoffman, K.-U. Münch, A. Leipertz, Opt. Lett. **21**, 525 (1996)
7. G. Kathryn, F. Frederik, and S. Jeffrey, in *51st AIAA Aerospace sciences meeting including the new horizons forum and aerospace exposition* (American Institute of Aeronautics and Astronautics, 2013)
8. W. Cai, C. F. Kaminski, in *nonlinear tomography: a new imaging concept*, 2014 (Optical Society of America), p. LM1D. 5
9. J. Li, Z. Du, T. Zhou, and K. Zhou, in *numerical investigation of two-dimensional imaging for temperature and species concentration using tunable diode laser absorption spectroscopy*, 2012 (IEEE), p. 234
10. M.G. Twynstra, K.J. Daun, Appl. Opt. **51**, 7059 (2012)
11. J. Song, Y. Hong, G. Wang, H. Pan, Appl. Phys. B **112**, 529 (2013)
12. W. Cai, C.F. Kaminski, Appl. Phys. Lett. **104**, 034101 (2014)
13. A. Guha, I.M. Schoegl, J. Propul. Power **30**, 350 (2014)
14. M. Wood, K. Ozanyan, IEEE Sens. J. **15**, 545 (2015)
15. W. Cai, C.F. Kaminski, Appl. Phys. Lett. **104**, 154106 (2014)
16. J. Hult, R.S. Watt, C.F. Kaminski, Opt. Express **15**, 11385 (2007)
17. C. Kaminski, R. Watt, A. Elder, J. Frank, J. Hult, Appl. Phys. B **92**, 367 (2008)
18. J. Langridge, T. Laurila, R. Watt, R. Jones, C. Kaminski, J. Hult, Opt. Express **16**, 10178 (2008)
19. T. Laurila, I. Burns, J. Hult, J. Miller, C. Kaminski, Appl. Phys. B **102**, 271 (2011)
20. R.S. Watt, T. Laurila, C.F. Kaminski, J. Hult, Appl. Spectrosc. **63**, 1389 (2009)
21. J. Hu, W. Bao, J. Chang, J. Propul. Power **30**, 1103 (2014)
22. W. Cai, D.J. Ewing, L. Ma, Comput. Phys. Commun. **179**, 250 (2008)
23. L. Ma, W. Cai, Appl. Opt. **47**, 4186 (2008)
24. W. Cai, L. Ma, Comput. Phys. Commun. **181**, 11 (2010)